ACS APPLIED MATERIALS & INTERFACES

Research Article

www.acsami.org

# Solid-State Fabrication of $SnS_2$/C Nanospheres for High-Performance Sodium Ion Battery Anode

Jingjing Wang,[‡] Chao Luo,[†] Jianfeng Mao,[†] Yujie Zhu,[†] Xiulin Fan,[†] Tao Gao,[†] Alice C. Mignerey,[‡] and Chunsheng Wang*,[†]

[†]Department of Chemistry and Biochemistry and [‡]Department of Chemical and Biomolecular Engineering, University of Maryland, College Park, Maryland 20742, United States

Supporting Information

**ABSTRACT:** Tin disulfide ($SnS_2$) has emerged as a promising anode material for sodium ion batteries (NIBs) due to its unique layered structure, high theoretical capacity, and low cost. Conventional $SnS_2$ nanomaterials are normally synthesized using hydrothermal method, which is time-consuming and difficult to scale up for mass production. In this study, we develop a simple solid-state reaction method, in which the carbon-coated $SnS_2$ ($SnS_2$/C) anode materials were synthesized by annealing metallic Sn, sulfur powder, and polyacrylonitrile in a sealed vacuum glass tube. The $SnS_2$/C nanospheres with unique layered structure exhibit a high reversible capacity of 660 mAh $g^{-1}$ at a current density of 50 mA $g^{-1}$ and maintain at 570 mAh $g^{-1}$ for 100 cycles with a degradation rate of 0.14% per cycle, demonstrating one of the best cycling performances in all reported $SnS_2$/C anodes for NIBs to date. The superior cycling stability of $SnS_2$/C electrode is attributed to the stable nanosphere morphology and structural integrity during charge/discharge cycles as evidenced by ex situ characterization.

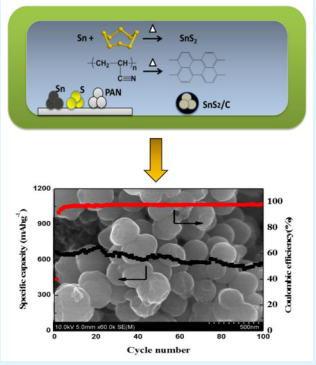


**KEYWORDS:** *tin disulfide, solid-state synthesis, nanospheres, anode, sodium-ion batteries, cycling stability*

## INTRODUCTION

As promising substitutions to lithium ion batteries, sodium ion batteries (NIBs) have attracted much attention for renewable energy storage due to low cost, inexhaustible sodium resources, and insertion chemistry similar to that of lithium ions.[1−4] The current NIBs face severe challenges from low energy density and poor cycling stability since sodium intercalation induces anisotropic volume expansion, which triggers particle pulverization and insufficient contact with the current collector.[5] Previous studies on the exploration of low-cost cathode materials, including selenium, $NaFePO_4$, transitional metal oxides, and sodium sulfate,[3,6−8] have achieved great success in the fabrication of high-performance cathode materials. The anode material studies focus on carbonaceous materials,[9−12] metals (Sn, Sb),[13−15] and metal oxides,[16,17] which suffer from either low capacity or poor cycle life. The exploration of advanced anode materials with high capacity and long cycle life has emerged as a primary bottleneck for the development of high-performance NIBs.

To pursue a high-performance anode material, the particle pulverization induced by sodium ion insertion/extraction must be alleviated. The layered structure is favorable for ion intercalation/deintercalation, and the interlayer spacing enables better accommodation upon large volume expansion. Among metal sulfides,[18−20] $SnS_2$ has a $CdI_2$-type structure with each layer stacking via van der Waals interactions.[21] Its large interlayer distance (0.59 nm) facilitates the intercalation/deintercalation of alkali metal ions ($Li^+$, $Na^+$), and it is considered a promising anode material for lithium and sodium storage.[22−27] Inspired by the similar two-dimensional structure of graphene, Xie et al. reported that $SnS_2$@graphene composite can provide a reversible capacity of 725 mAh $g^{-1}$ for 60 cycles at a current rate of 20 mA $g^{-1}$.[28] Recently, Zhang et al. reported $SnS_2$ with reduced graphene oxide composite for NIB anode, which can deliver a high charge capacity of 649 mAh $g^{-1}$ at a current rate of 100 mA $g^{-1}$. However, it still suffers from capacity loss after long-term cycling.[29] Meanwhile, the preparation of $SnS_2$/graphene composite involves the complex long-time hydrothermal synthesis of $SnS_2$ from $SnCl_4$ precursor, reduction of graphene oxide, and complicated purification process from the mixture of tin(IV) chloride, thioacetamide (TAA).[30] Therefore, it is not feasible for large-scale production of uniform nanomaterial.

Herein, for the first time, we synthesized carbon-coated $SnS_2$ nanomaterial using solid-state reaction in which metallic Sn, sulfur powder, and polyacrylonitrile (PAN) were annealed in a sealed vacuum glass tube. First, this synthetic route enables mass production of $SnS_2$/C nanomaterials. Second, the annealed $SnS_2$/C nanomaterials can be directly used for electrode preparation without further purification. Third, the large interlayer distance of $SnS_2$ synthesized using solid-state reaction can effectively accommodate the volume changes in the sodiation, and the carbon from carbonized PAN significantly improves the electrical conductivity of $SnS_2$. Our

Received: March 19, 2015
Accepted: May 13, 2015
Published: May 13, 2015




DOI: 10.1021/acsami.5b02413
ACS Appl. Mater. Interfaces 2015, 7, 11476−11481

experimental observations demonstrate that $SnS_2$/C nanomaterials show superior sodium storage capability with high reversible capacity (~600 mAh/g) after 100 deep galvanostatic cycles. Extensive results from ex situ scanning electron microscopy (SEM) show that the nanosphere morphology is maintained without obvious particle pulverization and aggregation, leading to high capacity retention after hundreds of charge/discharge cycles.

## RESULTS AND DISCUSSION

The $SnS_2$/C composite was synthesized via a facile solid-state reaction in a sealed glass tube under vacuum. As shown in Figure 1, metallic tin (Sn), sulfur powder, and PAN are mixed

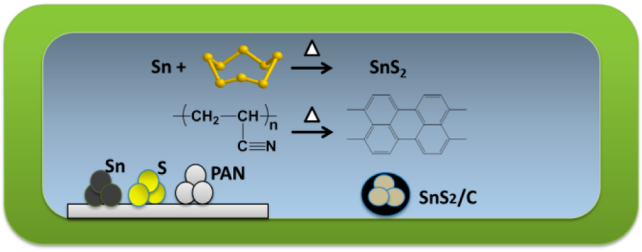


**Figure 1.** Schematic illustration of solid-state synthesis route of $SnS_2$/C nanomaterials.

in a sealed vacuum glass tube and annealed at 600 °C for 3 h. Tin disulfide ($SnS_2$) is formed on carbon matrix, which is generated by the carbonization of PAN. Since the melting point (231.9 °C) of metallic Sn is much lower than the boiling point (445 °C) of sulfur, gaseous sulfur at 600 °C can completely reacts with liquid Sn in the sealed tube to form $SnS_2$ and uniformly disperse on the carbon matrix formed from carbonization of PAN. By this method, $SnS_2$/C nanomaterials can be produced in large quantities with their composition precisely controlled.

The crystalline structure of $SnS_2$ was characterized using X-ray diffraction (XRD) pattern (Figure 2a). All the peaks can be indexed to 2T-type layered structure of $SnS_2$ (PDF 00–023–0677) with a calculated lattice parameter of $a$ = 3.162 ± 0.003 Å and $c$ = 5.890 ± 0.003 Å. The absence of impurity peaks indicates the formation of pure crystalline $SnS_2$. Since no graphite peak is observed in XRD, the carbon formed from carbonization of PAN exists as amorphous carbon. The graphitization degree of carbon in $SnS_2$/C was further characterized with Raman spectra as shown in Figure 2b. The typical Raman active $^1A_g$ mode of $SnS_2$ was observed as a sharp peak at 313 $cm^{-1}$, owing to in-plane vibrational modes within a sulfur–tin–sulfur plane.[31,32] The Raman spectra exhibit two broad bands at 1350 $cm^{-1}$ (D band) and 1600 $cm^{-1}$ (G band), corresponding to typical in-plane vibration of $sp^2$-bonded carbon atoms and vibrational modes from $sp^3$-bonded carbon atoms in amorphous carbon, respectively.[33] The intensity ratio of D/G band is 2/1 as demonstrated by Figure 2b. The high peak ratio of D band to G band demonstrates the low graphitization of carbon in $SnS_2$/C, which is consistent with the XRD result in Figure 2a. The $SnS_2$ content in $SnS_2$/C composite was determined using thermogravimetric analysis (TGA) as shown in Supporting Information, Figure S1. The major weight loss in the range of 450–600 °C is attributed to the combustion of C to $CO_2$ gas and the oxidation of $SnS_2$ to $SO_2$ gas when the sample was oxidized in air from 25 to 800 °C.[34] On the basis of the weight loss in TGA test and eq 1 (where Mw indicates molecular weight), the weight ratio of $SnS_2$ in the composite is calculated as 41%.

$$\mathrm{SnS_2(wt\%)} = 100 \times \frac{\mathrm{Mw\ of\ SnS_2}}{\mathrm{Mw\ of\ SnO_2}} \times \frac{\mathrm{mass\ of\ SnO_2}}{\mathrm{mass\ of\ SnS_2/C\ composite}} \quad (1)$$

The scanning electron microscopy (SEM) image (Figure 3a) reveals that the as-prepared $SnS_2$/C nanomaterial forms regular nanosphere morphology with a diameter of ~200 nm. This is because the carbonaceous material tends to form a regular spherelike morphology in the solid-state reaction. The spheroidizing of PAN also limits the growth of $SnS_2$ crystal in $c$-direction during the synthesis, thus forming nanospheres.[35] The nanosphere morphology of $SnS_2$/C composite is also demonstrated in transmission electron microscopy (TEM) image (Figure 3b) with clear round shape. The distribution of amorphous carbon, Sn, and S is further demonstrated by elemental mapping images of $SnS_2$/C as shown by Figure 4a–d. The energy-dispersive X-ray spectroscopy (EDS) confirms that $SnS_2$ is uniformly distributed in amorphous carbon matrix.

The electrochemical properties of $SnS_2$/C nanospheres are investigated in coin-cells using sodium metal as the counter electrode. To understand the discharge mechanism, cyclic voltammogram (CV) curves of $SnS_2$/C electrode were measured at a scanning rate of 0.1 mV/s during the initial

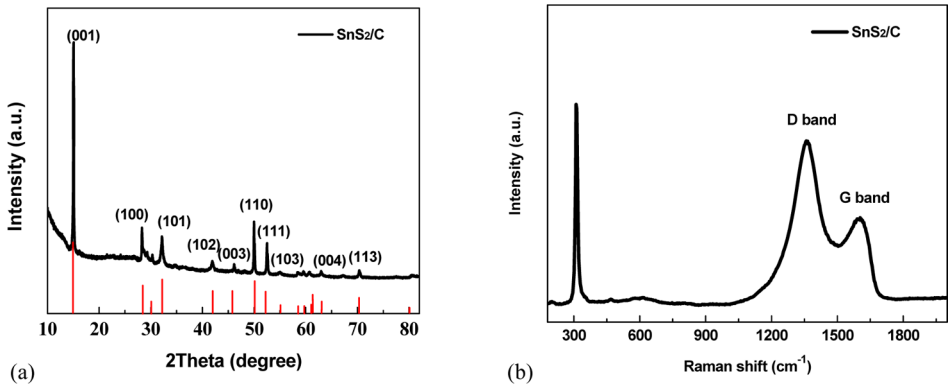


**Figure 2.** (a) XRD pattern of as-prepared $SnS_2$/C composite. (b) Raman spectra of $SnS_2$/C composite at room temperature using 532 nm wavelength excitation.



DOI: 10.1021/acsami.5b02413
ACS Appl. Mater. Interfaces 2015, 7, 11476–11481

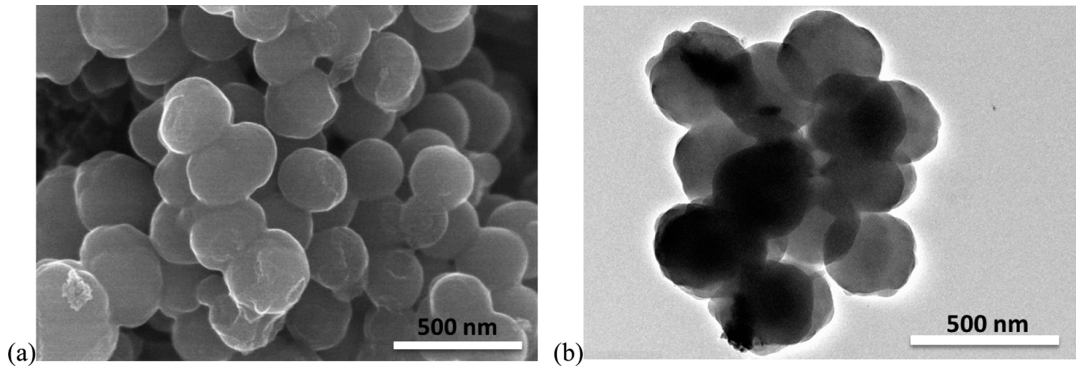


**Figure 3.** (a) SEM image of $SnS_2$/C composite; (b) TEM image of $SnS_2$/C composite.

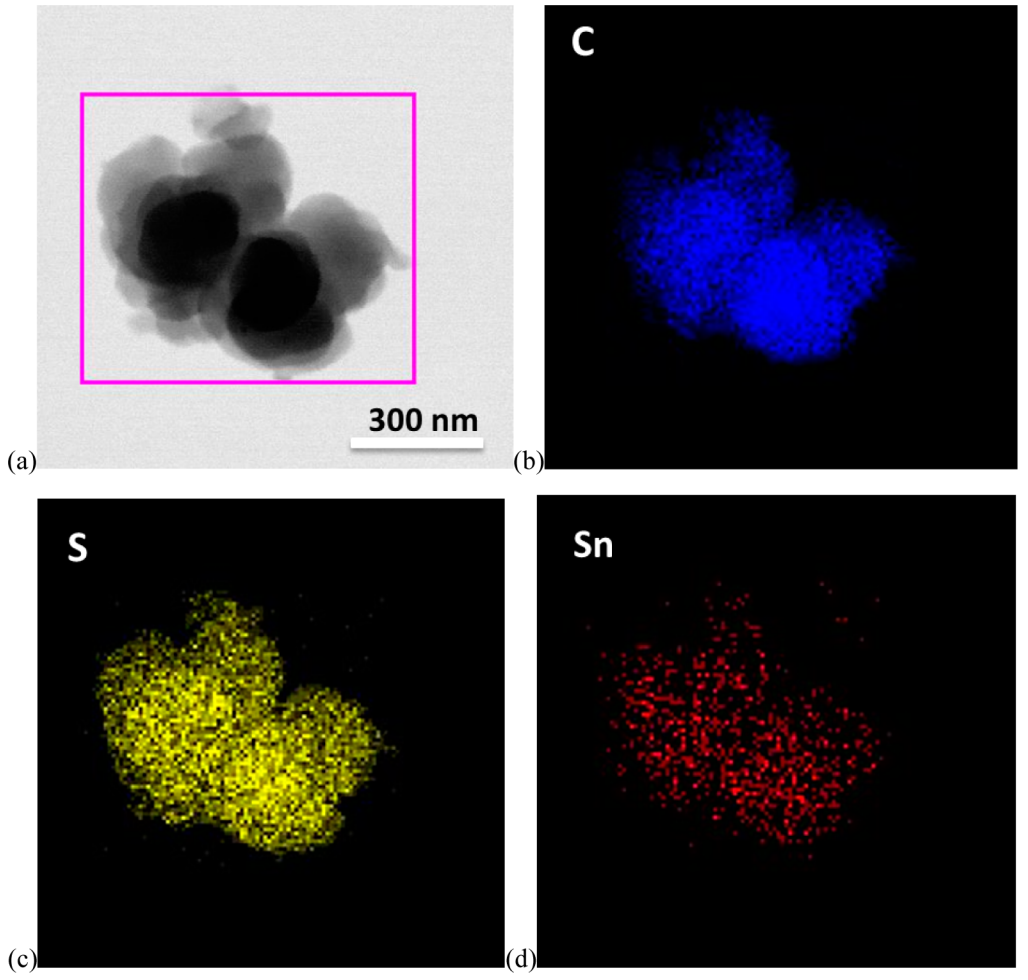


**Figure 4.** (a) EDS mapping image of $SnS_2$/C composite; (b) EDS mapping image of element C; (c) EDS mapping image of element S; (d) EDS mapping image of element Sn.

three cycles (Figure 5a). The initial sodiation process exhibits three cathodic peaks at 1.3, 0.9, and 0.25 V and a very small shoulder at 0.6 V. The peak at 1.3 V is ascribed to the formation of $Na_xSnS_2$ in which sodium ions intercalate into $SnS_2$ layers.[28,29] The peak at 0.9 V is due to the conversion reaction between $Na_xSnS_2$ and sodium ions ($Na_xSnS_2 + (4 - x)Na^+ \rightarrow Sn + 2Na_2S$), and the small shoulder at 0.6 V is due to the formation of irreversible solid electrolyte interphase (SEI) in the first cycle.[29] The peak at 0.25 V corresponds to the alloying process between metallic Sn and sodium ions ($Sn + yNa^+ \rightarrow Na_ySn$, $0 < y < 3.75$). During the anodic scan to 2.5 V, there are three corresponding oxidation peaks/shoulder at 0.3, 1.1, and 1.8 V due to the desodiation process. The oxidation peak at 0.3 V corresponds to desodiation process of $Na_xSn$ to form metallic Sn, and the peak at 1.1 V is attributed to the formation of $Na_xSnS_2$. The peak at 1.8 V corresponds to the deinsertion process of $Na_xSnS_2$. In the subsequent cycles, the reductive peak at 0.3 V shifts to higher potential at 0.45 V, which is attributed to activation process.

The galvanostatic charge and discharge behaviors of $SnS_2$/C electrode were measured between 0.005 and 2.5 V (Figure 5b) at a current density of 50 mA $g^{-1}$. During initial sodiation, the


DOI: 10.1021/acsami.5b02413
ACS Appl. Mater. Interfaces 2015, 7, 11476−11481

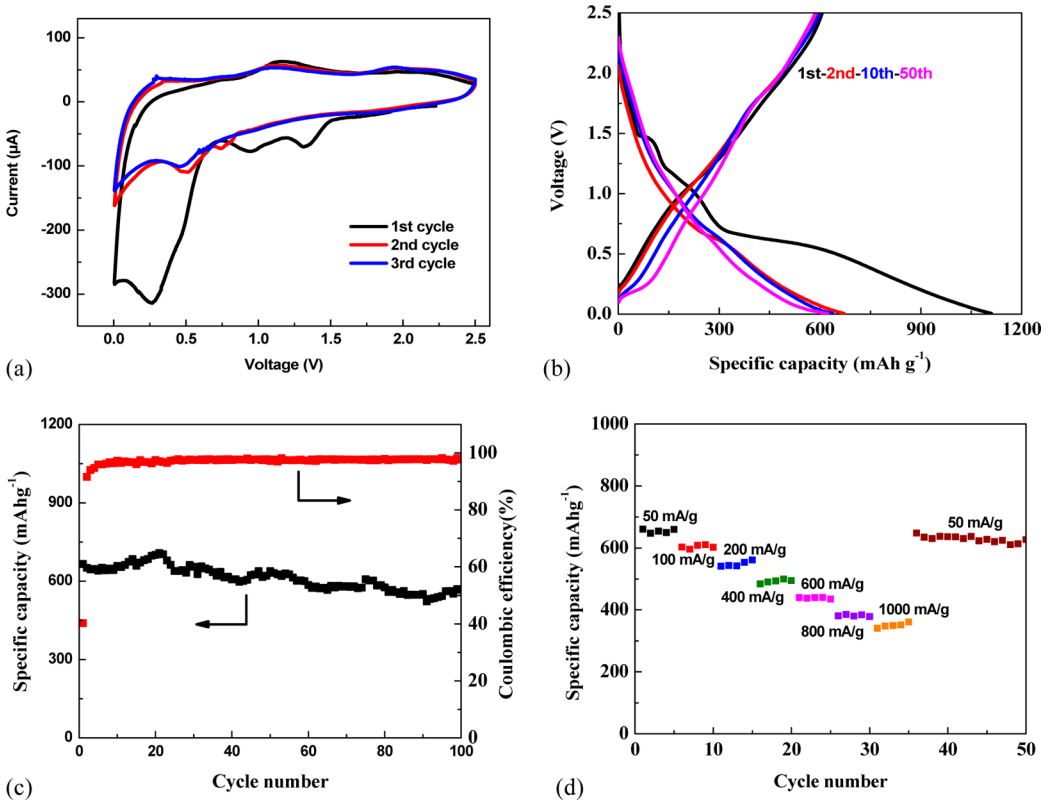


**Figure 5.** (a) Cyclic voltammetry curves of $SnS_2$/C electrode scanning from 5 mV to 2.5 V at a scanning rate of 0.1 mV/s. (b) Charge−discharge profiles of $SnS_2$/C electrode at a current density of 50 mA $g^{-1}$. (c) Cycling performance of $SnS_2$/C electrode at a current density of 50 mA $g^{-1}$. (d) Rate capability of $SnS_2$/C electrode at various current densities in NIBs.

plateau at higher voltage (1.4 V) is attributed to the intercalation of sodium ions into $SnS_2$ layers without composition change.[28,36] The slope plateau at 0.8−0.6 V corresponds to the conversion reaction between sodium ions and $Na_xSnS_2$, in which metallic Sn and $Na_2S$ are formed, and the formation of SEI due to reduction of electrolytes. A sloping curve is observed at a lower voltage, which is indicative of the alloying reaction between sodium ions and Sn ($Sn + yNa^+ \rightarrow Na_ySn$, $0 < y < 3.75$). $SnS_2$/C electrode delivers an extremely high capacity (1100 mAh $g^{-1}$) during the first sodiation, which is partially contributed by the irreversible formation of SEI layer. In the subsequent cycles, $SnS_2$/C electrode exhibits stable cycling performance, and a high reversible capacity (600 mAh/g) is maintained after 50 cycles as shown by the charge/discharge curves of cycles 2, 10, and 50. All the specific capacities are calculated based on $SnS_2$ after subtracting the contribution from carbon, which is ∼100 mAh $g^{-1}$ at the same current density (Supporting Information, Figure S2).

The electrochemical performance upon galvanostatic cycling between 0.005 and 2.5 V at a current density of 50 mA $g^{-1}$ is shown in Figure 5c. Though there is large irreversible capacity loss (60%) in the first discharge (sodiation) and charge (desodiation) due to the formation of SEI layer, $SnS_2$/C electrode displays a stable capacity of ∼600 mAh $g^{-1}$ for 100 cycles with capacity loss of 0.14% per cycles. Meanwhile, the Coulombic efficiency quickly increases to ∼100% after the first five cycles, demonstrating an efficient sodium ion intercalation/deintercalation process. The rate capability of $SnS_2$/C electrode at high current rates is demonstrated in Figure 5d. $SnS_2$/C electrode delivers stable charge capacity of 660 mAh $g^{-1}$ at 50 mA $g^{-1}$. With the current density increases to 1 A $g^{-1}$, the charge capacity still remains at 360 mAh $g^{-1}$. After the current density decreases to 50 mA $g^{-1}$, the capacity of $SnS_2$/C electrode recovers to its initial capacity immediately (660 mAh $g^{-1}$). The good rate capability of $SnS_2$/C electrode is an important indicator of its fast reaction kinetics in NIBs. The $SnS_2$/C nanospheres synthesized from solid-state reaction shows one of the best performances for NIB anodes to date.[28−30]

The mechanism for highly stable cycling behavior of $SnS_2$/C electrode was investigated by analysis of the electrochemical impedance spectroscopy (EIS) at cycles 1, 5, 10, and 50 (Figure 6) using equivalent circuit (inset in Figure 6). The fitted resistances are given in Supporting Information, Table S1. The EIS of $SnS_2$/C electrode is characterized by a depressed semicircle in high-frequency region and a straight sloping line in low-frequency region. The resistance at the intersection of high frequency represent electrolyte resistance ($R_1$), the semicircle corresponds to interface impedances (SEI impedance $R_2$ and charge transfer resistance $R_3$), and low-frequency slope line is due to the Li ion diffusion resistance in the $SnS_2$/C particles. As shown in Figure 6 and Supporting Information, Table S1, the interface resistance $R_2+R_3$ decrease in the first five cycles due to the activation process and then become stable after five cycles. The stable impedance between cycles 10 and 50 demonstrates the robustness of the stable SEI layer and the robust structural integrity during charge/discharge cycles.

The morphology of $SnS_2$/C electrode after 50 cycles was investigated by SEM. As shown in Figure 7, the regular spherical particles can be clearly observed underneath the thin SEI layer formed during the first sodiation. The result is further confirmed with TEM image of cycled $SnS_2$/C electrode as


DOI: 10.1021/acsami.5b02413
ACS Appl. Mater. Interfaces 2015, 7, 11476−11481

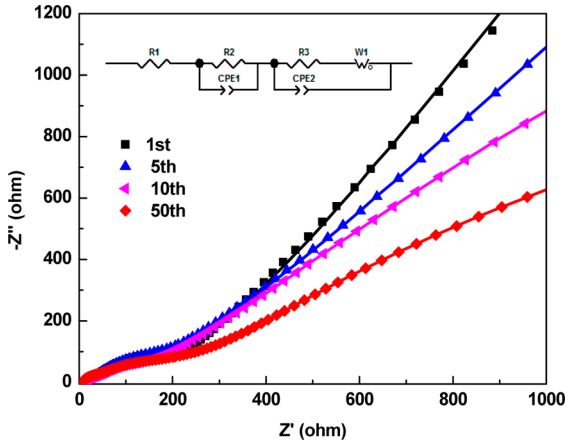


**Figure 6.** Experimental (dot) and simulated (line) electrochemical impedance spectra of $SnS_2$/C electrode after cycles 1, 5, 10, and 50 in NIBs.

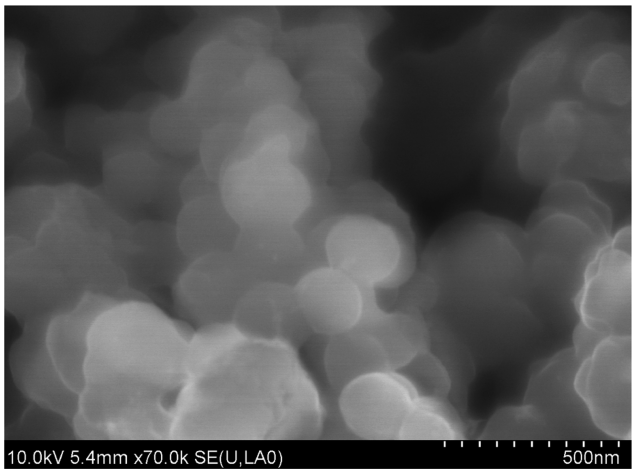


**Figure 7.** SEM image of $SnS_2$/C electrode after 50 charge/discharge cycles in NIBs.

shown in Supporting Information, Figure S4. It shows that $SnS_2$/C nanospheres maintain their morphology after 50 cycles, and the particle diameter also remained ~200 nm. There are no observable structural cracks, particle pulverization, or volume expansion induced by the large strain during repeated charge/discharge cycles. The result demonstrates that $SnS_2$/C electrode is able to maintain its structural and morphological integrity after cycling without severe particle pulverization, which contributes to the stable cycling performance in NIBs. Such feature makes the solid-state formed $SnS_2$/C nanospheres promising anode materials for high-performance NIBs.

## CONCLUSIONS

The $SnS_2$/C nanospheres were synthesized using solid-state reaction through annealing the mixture of metallic tin, sulfur powder, and PAN in sealing vacuum glass tube. The 41% of crystal $SnS_2$ nanoparticles are uniformly dispersed on carbon matrix to form 200 nm $SnS_2$/C composite sphere particles. The carbonization of PAN at high temperature provides a conductive carbon matrix to improve the electrical conductivity of $SnS_2$. The $SnS_2$/C anode can deliver a high specific capacity of 660 mAh $g^{-1}$ at 50 mA $g^{-1}$, maintain a reversible capacity of 570 mAh $g^{-1}$ after 100 cycles, and retain capacity of 360 mAh $g^{-1}$ even at 1 A $g^{-1}$. The $SnS_2$/C composite synthesized using solid-state reaction is robust to withstand the volume change during charge/discharge cycles as evidenced by the stable interface resistance in EIS analysis and good morphology maintenance after cycling in SEM images.

## EXPERIMENTAL SECTION

**Synthesis of $SnS_2$/C nanospheres.** All chemicals were purchased from Sigma-Aldrich and used as received. Tin, sulfur, and polyacrylonitrile (PAN) were mixed with a ratio of 2:3:5 (Sn/S/PAN) by weight and sealed in a glass tube under vacuum. The sealed glass tube was annealed in an oven at 600 °C for 3 h. $SnS_2$/Carbon composites were collected as black powder.

**Material Characterizations.** SEM images were taken by Hitachi SU-70 analytical ultrahigh resolution SEM (Japan); TEM images were taken by JEOL (Japan) 2100F field emission TEM; TGA was performed using a thermogravimetric analyzer (TA Instruments, USA) with a heating rate of 5 °C min 1 in argon; XRD pattern was recorded by Bruker Smart1000 (Bruker AXS Inc., USA) using Cu K$\alpha$ radiation; Raman measurements were performed on a Horiba Jobin Yvon Labram Aramis using a 532 nm diode-pumped solid-state laser, attenuated to give ~900 $\mu$W power at the sample surface.

**Electrochemical Measurements.** The as-prepared $SnS_2$/C powder was mixed with carbon black and sodium alginate binder to form slurry at the weight ratio of 80:10:10. Coin cells for NIBs were assembled with sodium foil as the counter electrode, 1 M $NaPF_6$ in a mixture of fluoroethylene carbonate/dimethyl carbonate (FEC/DMC, 1:1 by volume) as the electrolyte and Celgard 3501 as the separator. Electrochemical performance was tested using Arbin battery test station (BT2000, Arbin Instruments, USA). Both the charge and discharge current density and specific capacity were calculated based on the mass of $SnS_2$ in the electrode. CVs were recorded using Solatron 1260/1287 Electrochemical Interface (Solatron Metrology, UK) with a scan rate of 0.1 mV/s between 0.005 and 2.5 V (vs Na/$Na^+$).

## ASSOCIATED CONTENT

### Supporting Information

TGA results, cycling performance, XRD patterns, TEM image of electrode, circuit resistance versus cycle number. The Supporting Information is available free of charge on the ACS Publications website at DOI: 10.1021/acsami.5b02413.

## AUTHOR INFORMATION

### Corresponding Author

*E-mail: cswang@umd.edu.

### Notes

The authors declare no competing financial interest.

## ACKNOWLEDGMENTS

We acknowledge the financial support from CHBE/NSF Award No. 1438198. We also acknowledge the support of the Maryland NanoCenter and its NispLab. The authors are grateful for the technique help from Prof. K. Xu, H. Bai, J. Hu, and Prof. S.-B. Lee.

## REFERENCES

(1) Palomares, V.; Serras, P.; Villaluenga, I.; Hueso, K. B.; Carretero-González, J.; Rojo, T. Na-Ion Batteries, Recent Advances and Present Challenges to Become Low Cost Energy Storage Systems. *Energy Environ. Sci.* **2012**, *5*, 5884−5901.

(2) Ong, S. P.; Chevrier, V. L.; Hautier, G.; Jain, A.; Moore, C.; Kim, S.; Ma, X.; Ceder, G. Voltage, Stability and Diffusion Barrier Differences Between Sodium-Ion and Lithium-Ion Intercalation Materials. *Energy Environ. Sci.* **2011**, *4*, 3680−3681.

(3) Luo, C.; Xu, Y.; Zhu, Y.; Liu, Y.; Zheng, S.; Liu, Y.; Langrock, A.; Wang, C. Selenium@Mesoporous Carbon Composite with Superior



DOI: 10.1021/acsami.5b02413
*ACS Appl. Mater. Interfaces* 2015, 7, 11476−11481

Lithium and Sodium Storage Capacity. *ACS Nano* **2013**, *9*, 8003−8010.
(4) Xie, M.; Luo, R.; Lu, J.; Chen, R.; Wu, F.; Wang, X.; Zhan, C.; Wu, H.; Albishri, H. M.; Al-Bogami, A. S.; El-Hady, D. A.; Amine, K. Synthesis-Microstructure-Performance Relationship of Layered Transition Metal Oxides as Cathode for Rechargeable Sodium Batteries Prepared by High-Temperature Calcination. *ACS Appl. Mater. Interfaces* **2014**, *6*, 17176−17183.
(5) Wang, J. W.; Liu, X. H.; Mao, S. X.; Huang, J. Y. Microstructural Evolution of Tin Nanoparticles during in situ Sodium Insertion and Extraction. *Nano Lett.* **2012**, *12*, 5897−5902.
(6) Oh, S. M.; Myung, S. T.; Hassoun, J.; Scrosati, B.; Sun, Y. K. Reversible $NaFePO_4$ Electrode for Sodium Secondary Batteries. *Electrochem. Commun.* **2012**, *22*, 149−152.
(7) Xin, S.; Yin, Y.; Guo, Y.; Wan, L. A High-Energy Room-Temperature Sodium-Sulfur Battery. *Adv. Mater.* **2014**, *26*, 1261−1265.
(8) Jiang, Y.; Hu, M.; Zhang, D.; Yuan, T.; Sun, W.; Xu, B.; Yan, M. Transition Metal Oxides for High Performance Sodium Ion Battery Anodes. *Nano Energy* **2014**, *5*, 60−66.
(9) Song, H.; Li, N.; Cui, H.; Wang, C. Enhanced Storage Capability and Kinetic Processes by Pores- and Hetero-Atoms- Riched Carbon Nanobubbles for Lithium-Ion and Sodium-Ion Batteries Anodes. *Nano Energy* **2014**, *4*, 81−87.
(10) Hong, K.; Qie, L.; Zeng, R.; Yi, Z.; Zhang, W.; Wang, D.; Yin, W.; Wu, C.; Fan, Q.; Zhang, W.; Huang, Y. Biomass Derived Hard Carbon Used as a High Performance Anode Material for Sodium Ion Batteries. *J. Mater. Chem. A* **2014**, *2*, 12733−12738.
(11) Cao, Y.; Xiao, L.; Sushko, M. L.; Wang, W.; Schwenzer, B.; Xiao, J.; Nie, Z.; Saraf, L. V.; Yang, Z.; Liu, J. Sodium Ion Insertion in Hollow Carbon Nanowires for Battery Applications. *Nano Lett.* **2012**, *12*, 3783−3787.
(12) Ding, J.; Wang, H.; Li, Z.; Kohandehghan, A.; Cui, K.; Xu, Z.; Zahiri, B.; Tan, X.; Lotfabad, E.; Olsen, B. C.; Mitlin, D. Carbon Nanosheet Frameworks Derived from Peat Moss as High Performance Sodium Ion Battery Anodes. *ACS Nano* **2013**, *7*, 11004−11015.
(13) Oh, S. M.; Myung, S. T.; Jang, M. W.; Scrosati, B.; Hassoun, J.; Sun, Y. K. An Advanced Sodium-Ion Rechargeable Battery Based on a Tin−Carbon Anode and a Layered Oxide Framework Cathode. *Phys. Chem. Chem. Phys.* **2013**, *15*, 3827−3833.
(14) Zhu, H.; Jia, Z.; Chen, Y.; Weadock, N.; Wan, J.; Vaaland, O.; Han, X.; Li, T.; Hu, L. Tin Anode for Sodium-Ion Batteries Using Natural Wood Fiber as a Mechanical Buffer and Electrolyte Reservoir. *Nano Lett.* **2013**, *13*, 3093−3100.
(15) He, M.; Kravchyk, K.; Walter, M.; Kovalenko, M. V. Monodisperse Antimony Nanocrystals for High-Rate Li-ion and Naion Battery Anodes: Nano versus Bulk. *Nano Lett.* **2014**, *14*, 1255−1262.
(16) Jiang, Y.; Hu, M.; Zhang, D.; Yuan, T.; Sun, W.; Xu, B.; Yan, M. Transition Metal Oxides for High Performance Sodium Ion Battery Anodes. *Nano Energy* **2014**, *5*, 60−66.
(17) Deng, C.; Zhang, S.; Dong, Z.; Shang, Y. 1D Nanostructured Sodium Vanadium Oxide as a Novel Anode Material for Aqueous Sodium Ion Batteries. *Nano Energy* **2014**, *4*, 49−55.
(18) Wang, J.; Luo, C.; Gao, T.; Langrock, A.; Mignerey, A. C.; Wang, C. An Advanced $MoS_2$ /Carbon Anode for High-Performance Sodium-Ion Batteries. *Small* **2015**, *11*, 473−481.
(19) Wu, L.; Hu, X.; Qian, J.; Pei, F.; Wu, F.; Mao, R.; Ai, X.; Yang, H.; Cao, Y. A Sn−SnS−C Nanocomposite as Anode Host Materials for Na-Ion Batteries. *J. Mater.Chem. A* **2013**, *1*, 7181−7184.
(20) Yu, D. Y.; Prikhodchenko, P. V.; Mason, C. W.; Batabyal, S. K.; Gun, J.; Sladkevich, S.; Medvedev, A. G.; Lev, O. High-Capacity Antimony Sulphide Nanoparticle-Decorated Graphene Composite as Anode for Sodium-Ion Batteries. *Nat. Commun.* **2013**, *4*, 2922−2929.
(21) Luo, B.; Fang, Y.; Wang, B.; Zhou, J.; Song, H.; Zhi, L. Two Dimensional Graphene−$SnS_2$ Hybrids with Superior Rate Capability for Lithium Ion Storage. *Energy Environ. Sci.* **2012**, *5*, 5226−5230.
(22) Liu, Y.; Kang, H.; Jiao, L.; Chen, C.; Cao, K.; Wang, Y.; Yuan, H. Exfoliated-$SnS_2$ Restacked on Graphene as a High-Capacity, High-Rate, and Long-Cycle Life Anode for Sodium Ion Batteries. *Nanoscale* **2015**, *7*, 1325−1332.
(23) Liu, S.; Lu, X.; Xie, J.; Cao, G.; Zhu, T.; Zhao, X. Preferential c-Axis Orientation of Ultrathin $SnS_2$ Nanoplates on Graphene as High-Performance Anode for Li-Ion Batteries. *ACS Appl. Mater. Interfaces* **2013**, *5*, 1588−1595.
(24) Qu, B.; Ma, C.; Ji, G.; Xu, C.; Xu, J.; Meng, Y. S.; Wang, T.; Lee, J. Y. Layered $SnS_2$-Reduced Graphene Oxide Composite - A High-Capacity, High-Rate, and Long-Cycle Life Sodium-Ion Battery Anode Material. *Adv. Mater.* **2014**, *26*, 3854−3859.
(25) Chen, P.; Su, Y.; Liu, H.; Wang, Y. Interconnected Tin Disulfide Nanosheets Grown on Graphene for Li-Ion Storage and Photocatalytic Applications. *ACS Appl. Mater. Interfaces* **2013**, *5*, 12073−12082.
(26) Liu, Z.; Deng, H.; Mukherjee, P. P. Evaluating Pristine and Modified $SnS_2$ as a Lithium-Ion Battery Anode: A First-Principles Study. *ACS Appl. Mater. Interfaces.* **2015**, *7*, 4000−4009.
(27) Wang, G.; Peng, J.; Zhang, L.; Zhang, J.; Dai, B.; Zhu, M.; Xia, L.; Yu, F. Two-Dimensional $SnS_2$@PANI Nanoplates with High Capacity and Excellent Stability for Lithium-ion Batteries. *J. Mater. Chem. A* **2015**, *3*, 3659−3666.
(28) Xie, X.; Su, D.; Chen, S.; Zhang, J.; Dou, S.; Wang, G. $SnS_2$ Nanoplatelet@Graphene Nanocomposites as High-Capacity Anode Materials for Sodium-Ion Batteries. *Chem.—Asian J.* **2014**, *9*, 1611−1617.
(29) Zhang, Y.; Zhu, P.; Huang, L.; Xie, J.; Zhang, S.; Cao, G.; Zhao, X. Few-Layered $SnS_2$ on Few-Layered Reduced Graphene Oxide as Na-Ion Battery Anode with Ultralong Cycle Life and Superior Rate Capability. *Adv. Funct. Mater.* **2015**, *25*, 481−489.
(30) Zhou, T.; Pang, W.; Zhang, C.; Yang, J.; Chen, Z.; Liu, H. K.; Guo, Z. Enhanced Sodium-Ion Battery Performance by Structural Phase Transition from Two-Dimensional Hexagonal-$SnS_2$ to Orthorhombic-SnS. *ACS Nano* **2014**, *8*, 8323−8333.
(31) Mead, D. G.; Irwin, J. C. Raman Spectra of $SnS_2$ and $SnSe_2$. *Solid State Commun.* **1976**, *20*, 885−887.
(32) Wang, C.; Tang, K.; Yang, Q.; Qian, Y. Raman Scattering, Far Infrared Spectrum and Photoluminescence of $SnS_2$ Nanocrystallites. *Chem. Phys. Lett.* **2002**, *357*, 371−375.
(33) Sevilla, M.; Fuertes, A. B. The Production of Carbon Materials by Hydrothermal Carbonization of Cellulose. *Carbon* **2009**, *47*, 2281−2289.
(34) Bissessur, R.; Schipper, D. Exfoliation and Reconstruction of $SnS_2$ Layers: A Synthetic Route for the Preparation of Polymer-$SnS_2$ Nanomaterials. *Mater. Lett.* **2008**, *62*, 1638−1641.
(35) Sun, X.; Li, Y. Hollow Carbonaceous Capsules from Glucose Solution. *J. Colloid Interface Sci.* **2005**, *291*, 7−12.
(36) Wu, Q.; Jiao, L.; Du, J.; Yang, J.; Guo, L.; Liu, Y.; Wang, Y.; Yuan, H. One-Pot Synthesis of Three-Dimensional $SnS_2$ Hierarchitectures as Anode Material for Lithium-Ion Batteries. *J. Power Sources* **2013**, *239*, 89−93.


DOI: 10.1021/acsami.5b02413
*ACS Appl. Mater. Interfaces* 2015, 7, 11476−11481